Optimized kinematics enable both aerial and aquatic propulsion from a single three-dimensional flapping wing

Jacob S. Izraelevitz, Miranda Kotidis, and Michael S. Triantafyllou[*]
Massachusetts Institute of Technology, Cambridge, Massachusetts 02139, USA

Flapping wings in nature demonstrate a large force envelope, with capabilities far beyond the traditional limits of static airfoil section coefficients. Puffins, murres, and other auks particularly showcase this effect, as they are able to generate both enough thrust to swim and enough lift to fly, using the same wing, purely by changing the wing motion trajectory. The wing trajectory is therefore an additional design criterion to be optimized along with traditional aircraft parameters and could open the door to dual aerial-aquatic robotic vehicles. In this paper we showcase one realization of a three-dimensional flapping-wing actuation system that reproduces the force coefficients necessary for dual aerial-aquatic flight. The wing apparatus oscillates by the root and employs an active upstream and downstream sweep degree of freedom. We analyze two types of motions in detail: aerial motions where the wing tip moves upstream during the power stroke of each flapping cycle and aquatic motions where the wing tip moves downstream during the power stroke. We design these aerial and aquatic flapping-wing trajectories using an experiment-coupled optimization routine, allowing control of the unsteady forces throughout each flapping cycle. Additionally, we elucidate the wakes of these complex wing trajectories using dye visualization, correlating the wake vortex structures with simultaneous experiment force measurements. After optimization, the wing trajectories generate the large force envelope necessary for propulsion in both fluid media and furthermore demonstrate improved control over the unsteady wake.

I. INTRODUCTION

Flapping wings, whereby a large lifting surface oscillates independently of the body motion, have many advantages over standard fixed-wing vehicles. Using an oscillating wing to produce thrust yields an efficiency which is comparable to the best propellers [1], yet can simultaneously be used as a control surface by appropriately timing the various wing degrees of freedom [2].

Over the past several decades, numerous rich engineering insights into the design of flapping propulsors have been derived from studies of natural swimmers and fliers. For example, most animals operate their wings within a narrow range of nondimensional frequencies [3–5] that correlate well with engineering experiments of flapping airfoils [1]. Furthermore, a flapping airfoil efficiently generates thrust through the creation of a reverse von Kármán vortex street wake [6]; a vortex pattern that has also been noted in fish swimming [7]. Other experiments have introduced additional parameters to the flapping motion in order to improve performance. Examples include adding spanwise flexibility to the foil [8], investigating three-dimensional effects [9], and adapting the angle-of-attack profile beyond simple sinusoids [10]. Maneuvers can be obtained by breaking the
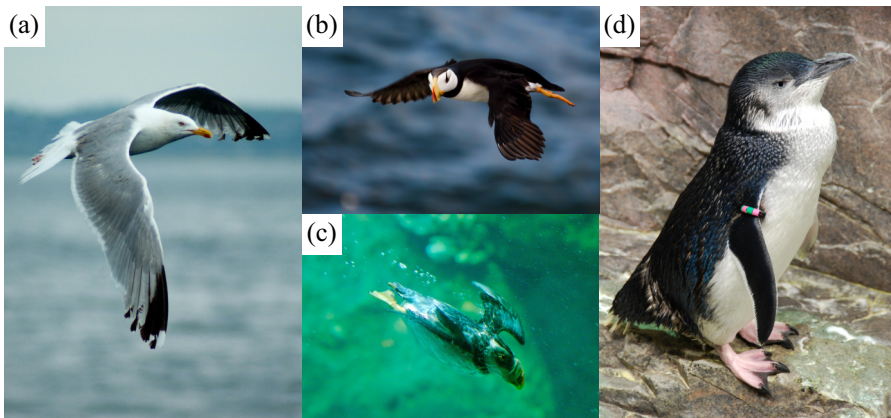
---

[*]mistetri@mit.edu

FIG. 1. Comparison of actuator areas in aerial and aquatic avians. Dual aerial-aquatic wings are of intermediate planform size compared to larger flying-only wings and smaller swimming-only wings. Selected birds have approximately equal body mass, ranging from 500 to 1500 g. Photographs show (a) European Herring Gull *Larus argentatus* [22] with flying-only wings, (b) and (c) Horned Puffin *Fratercula corniculata* both flying [23] and swimming [24] using dual aerial-aquatic wings, and (d) Little Blue Penguin *Eudyptula minor* [25] with swimming-only wings. Photos were reproduced under Creative Commons (see [22–25]).

symmetry of the foil motion, such as an offset in the pitching angle [2], to bias the lift. For a thorough review, we refer the reader to Triantafyllou *et al.* [11].

One additional pertinent insight, unique to extreme motions of the lifting surface, is that a flapping wing can choose the magnitude and direction of the wing-relative flow velocity [12]. These wing kinematics are generally parametrized with a variable stroke angle, whereby the animal tilts the plane of wing motion. Examples of variable stroke angles are widespread throughout the animal literature, such as birds [13], bats [14], dragonflies [15], turtles [16], and even mollusks [17]. Prior engineering experiments by Izraelevitz and Triantafyllou [18,19] illustrated that the stroke angle, in two-dimensional planar motion or three-dimensional flapping, respectively, can provide a pulsed force that is oriented in an intended direction. This strategy vastly increases the reachable force envelope of the wing.

In fact, perhaps the best natural examples of this wide reachable force envelope are puffins, murres, and other auks: flying birds that use wing-propelled swimming to chase prey. These organisms use the same wings to provide both enough lift for flight and the required underwater thrust to overcome their body drag. Such dual-purpose wings represent a metabolic compromise [20] and Pennycuick [21] notes that they are of the intermediate planform area between purely flying and purely swimming birds (Fig. 1) of the same mass. Unsurprisingly, an ideal aerial flapping wing is too large underwater and an ideal aquatic flapping wing is too small for air. Instead, a dual-purpose wing must compensate for its flawed planform size by using wing motion. Auks thereby illustrate that a flapping wing, if given enough control of its motion, is more than capable of generating the force envelope required for flight through both air and water. The difficulty is in developing the wing trajectories.

In this paper, our primary aim is to verify experimentally that by changing the wing trajectory alone, the force envelope from a single flapping wing can be expanded to allow both enough lift for aerial weight support and the thrust for underwater travel. Inspired by auk propulsion, controlling the stroke angle is our principal method of obtaining the necessary large force envelope. Several species of auks are indeed known to change their stroke angle between flying and swimming [26–28], consistent with this technique. Our experimental wing is of finite span with a mounted force transducer, oscillates about the root at an inclined stroke angle, and employs actively controlled pitch along the span.

As the second main contribution of this work, we also include a simple experiment-based optimization routine to derive the motion parameters. In such experimental analogs of avian motions,
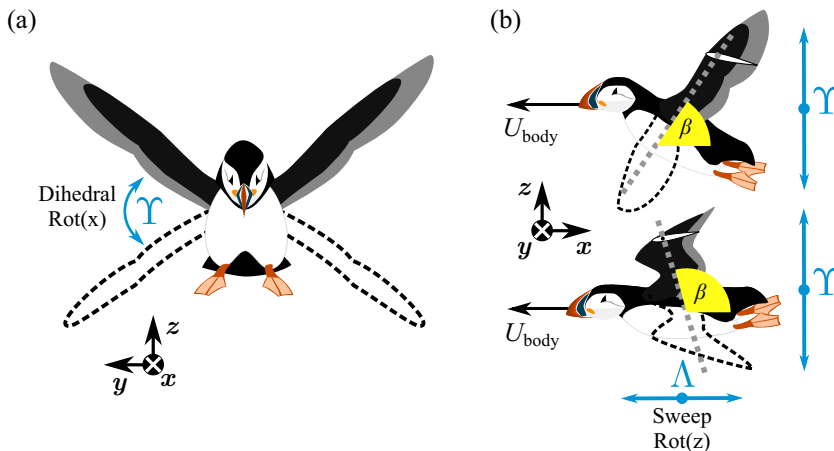
FIG. 2. Dihedral, sweep, and stroke angles in auks. Auks, similar to many other birds, move their wings at an inclined stroke angle, which combines both dihedral and sweep motion. (a) Dihedral Υ as seen from the front. (b) Sweep Λ and stroke angle β as seen from the side. The stroke angle can be greater or less than $90°$. Animal art has been modified from public domain content [29].

the design of suitable wing kinematics is difficult to perform *a priori*. Strong wake vorticity produces an unknown inflow which affects the angle of attack of the wing, complicating any attempt to produce a specific desired force profile. A controlled stroke angle further amplifies the complexity of ideal kinematics, as simple sinusoidal joint motion definitions do not necessarily produce clean force outputs [18]. However, by alternating between recording experimental transducer forces and applying automated corrections to the wing motions, we manipulate the kinematics to provide unidirectional force in an intended direction each flapping cycle.

Finally, we also record dye visualization of our wake structures, as optimized kinematics are required chiefly to offset wake effects that are initially unknown. Future investigations and advanced modeling of these wake geometries will inform better force models, eventually mitigating the need for closed-loop optimization of the kinematics. We show that the two-dimensional planar wakes and phenomena discussed by Izraelevitz and Triantafyllou [18] are expandable, with caveats, to three-dimensional wings.

II. MOTIVATION

A. Stroke angle

While wing motion data on flying and swimming auks is rare compared to other birds, they are known to substantially change their flapping trajectory between the two fluid media. Figure 2 illustrates the kinematics of one such example, the stroke angle in Atlantic puffins (*Fratercula arctica*) when both flying [26] and swimming [27].

In the frame of reference of the bird, the tip of a flapping wing usually moves up and down [also known as wing dihedral Υ in Fig. 2(a)], but also includes additional motion forward and backward [also known as wing sweep Λ in Fig. 2(b)] relative to the flow. The exact motions are often complex, but a common simplification is to assume that the wings move only in a single flat plane, tilted from the horizontal by the stroke angle β [14,17,30] to simultaneously include both the dihedral and sweep motions.

The avian wing motion is further generally divided into two parts: the first half of the dihedral flapping cycle, the downstroke or power stroke, followed by the the second half, the upstroke or recovery stroke. In most birds, with the notable exemption of penguins, the downstroke has more force

Instantaneous Forces

Mean Forces

(a) Fast Flight
$\beta \approx 90°$

Wing-tip Motion

Force

U_{body}

β

(b) Slow Flight
$\beta < 90°$

β

(e) Aerial Forces

$A_{parasitic}$

$S_{air}/2$

$F_{z,air}$

T_{air}

$D_{air} = D_{parasitic} + D_{induced}$

mg

(c) Shallow Swim
$\beta > 90°$

β

(d) Deep Swim
$\beta > 90°$

z

y x

β

(f) Aquatic Forces

$S_{water}/2$
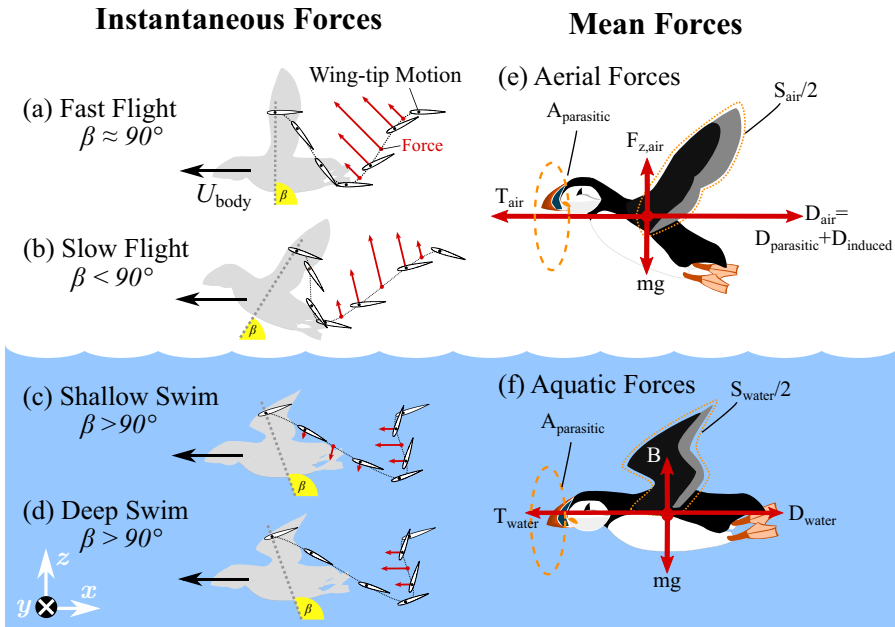
$A_{parasitic}$

B

T_{water}

D_{water}

mg

FIG. 3. Stroke angle control. (a)–(d) Variable stroke angles β of the wing tip observed in auks with a variety of flying and swimming gaits, along with the vectorial force throughout the flapping cycle. (e) and (f) Mean forces on the auk in air and water, produced by both the wings and the environment. Animal art has been modified from public domain content [29] and airfoil trajectories with permission from Izraelevitz and Triantafyllou [18].

than the upstroke, as the downstroke flight muscles are necessarily stronger than the supracoracoid recovery muscles, even in auks [28,31].

Due to this asymmetry, the stroke angle acts as a method to vector the fluid force in avian flight. The stroke angle chooses the magnitude and direction of the flow during the downstroke, and as the lift is perpendicular to the direction of fluid flow, the stroke angle thereby chooses the force. Figure 3 describes four trajectories in detail that highlight this phenomenon.

(a) Fast-flying birds [Fig. 3(a)] have an almost vertical stroke angle ($\beta \cong 90°$), so the wing-tip motion is sinusoidal in the dorsal-ventral plane [13]. This orientation of the wing motion allows the downstroke to provide a net force (highlighted in red) that contains both a vertical component to offset the weight and a large thrust component to fight aerodynamic drag.

(b) Slow-flying animals [Fig. 3(b)] [13–15], including puffins [26], are known to sweep the wings forwards ($\beta < 90°$) during the downstroke. As the bird moves at speed U_{body}, the wing tip now follows a skewed sinusoid in a global reference frame. Flying slowly is challenging because the available lift decreases, while the weight requirement stays the same. Using a forward-moving downstroke therefore has two advantages: The flow speed as seen by the wing increases and the flow direction is primarily horizontal. As a result, this wing motion boosts the vertical force while still providing the small requisite thrust, allowing the animal to fly at the slow airspeeds that would otherwise be out of reach.

(c) When swimming [Fig. 3(c)], on the other hand, auks instead sweep their wings backward (downstream, $\beta > 90°$) during the downstroke. This behavior, seen in the Atlantic puffin [27], the common murre (*Uria aalge*) [28], and pigeon guillemots (*Cepphus Columba*) [32], tilts the oncoming flow during the downstroke so that the instantaneous lift is angled more towards thrust. However, as seabirds are positively buoyant, the upstroke is slightly active [27,31,33] (though less than the downstroke) to counteract this buoyancy when swimming level or to add bonus thrust if required.

(d) At depths exceeding approximately 10 m [Fig. 3(d)], however, this upstroke force disappears due to a buoyancy change [31,32]. Unlike a rigid-hull vessel, diving birds have air trapped in their nonrigid lungs and feathers which compress at depth [34], lowering their displaced volume. An auk's buoyancy therefore decreases during deeper dives and accordingly their wing flapping becomes more downstroke biased [31,32]. Furthermore, an inactive upstroke lowers the amount of unwanted oscillation [12,18] perpendicular to the direction of travel, generally considered detrimental to maintaining an intended forward course. In contrast, for aquatic-only birds such as penguins, symmetry between upstroke and downstroke is much more prevalent at all depths given their different musculature [31].

For the purposes of this paper, we will focus on trajectories that are downstroke biased at various stroke angles [i.e., motions in Figs. 3(a), 3(b), and 3(d)] as the targets for optimization of the wing kinematics, as they are most consistent with the force directionality required for aerial-aquatic operation. This asymmetry between the upstroke and downstroke appears to be the rule rather than the exception.

B. Aerial-aquatic force coefficients

Beyond changing the direction of the fluid force, a dual aerial-aquatic wing must also provide mean force coefficients that differ by an order of magnitude. The aerial constraint of maintaining lift directly conflicts with the low-drag requirements of efficient underwater locomotion. This design compromise is easily elucidated by the following mathematical exercise, where we derive a scaling ratio C^* to quantify the force envelope requirement.

First, we nondimensionalize the forces as

$$C_x(t) = -C_T(t) = \frac{2F_x(t)}{\rho S U^2}, \quad C_y(t) = \frac{2F_y(t)}{\rho S U^2}, \quad C_z(t) = \frac{2F_z(t)}{\rho S U^2}, \tag{1}$$

where S is the total planform area of the two wings, ρ is the fluid density, and U is the forward speed. Note we use $C_z(t)$ rather than $C_L(t)$ to avoid confusion with the instantaneous lift direction. Next, given a hypothesized vehicle of mass m traveling in air at velocity U_{air} as described in Fig. 3(e), we note that to obtain weight support, the vertical force must equal the weight mg,

$$mg = F_{z,\text{air}} = \tfrac{1}{2} \rho_{\text{air}} U_{\text{air}}^2 S_{\text{air}} \bar{C}_{z,\text{air}}, \tag{2}$$

where an overbar, such as in $\bar{C}_{z,\text{air}}$, denotes the average of a time-varying quantity over the flapping cycle. The aerial vertical force $\bar{F}_{z,\text{air}}$ comes at the cost of some total drag $\bar{D}_{\text{air}}$ overcome by the flapping wings, a fraction of which is due to no-lift drag losses on the fuselage $\bar{D}_{\text{parasitic}}$,

$$\bar{D}_{\text{parasitic}} = k_{\text{parasitic}} \bar{D}_{\text{air}}, \tag{3}$$

$$\tfrac{1}{2} \rho_{\text{air}} U_{\text{air}}^2 A_{\text{parasitic}} \bar{C}_{D,\text{parasitic}} = k_{\text{parasitic}} \tfrac{1}{2} \rho_{\text{air}} U_{\text{air}}^2 S_{\text{air}} \bar{C}_{D,\text{air}}, \tag{4}$$

$$A_{\text{parasitic}} \bar{C}_{D,\text{parasitic}} = k_{\text{parasitic}} S_{\text{air}} \bar{C}_{D,\text{air}}, \tag{5}$$

where $\bar{C}_{D,\text{parasitic}}$, $\bar{C}_{D,\text{air}}$, and $A_{\text{parasitic}}$ are the mean nondimensional drag coefficients, reference areas, and $k_{\text{parasitic}} < 1$ is the fraction of the drag in air devoted to the parasitic drag losses.

Rather surprising, a flying-swimming vehicle can operate at roughly the same Reynolds number $\text{Re} = Uc/\nu$ in both fluids, conveniently allowing the use of the same fuselage drag coefficient $\bar{C}_{D,\text{parasitic}}$ underwater. The ratio of kinematic viscosity between the air and water at sea level is $\nu_{\text{air}}/\nu_{\text{water}} \cong 12$ [35]; therefore, assuming a flight speed of 12 times faster in air [36] and the same chord length c, the Reynolds numbers in both fluids are identical. This observation is also consistent with observations of the swimming and flying velocities of a number of auk species [21,28,37]

$$\frac{U_{\text{air}} c}{\nu_{\text{air}}} = \text{Re}_{\text{air}} \cong \text{Re}_{\text{water}} = \frac{U_{\text{water}} c}{\nu_{\text{water}}}. \tag{6}$$

For an underwater vehicle of neutral buoyancy [such as an auk during a deep dive, Fig. 3(f)] at this same Reynolds number, the thrust coefficient from the wings must only match the parasitic drag coefficient as no mean lift is required,

$$\bar{T}_{\text{water}} = \bar{D}_{\text{water}}, \tag{7}$$

$$\tfrac{1}{2}\rho_{\text{water}}U_{\text{water}}^2 S_{\text{water}}\bar{C}_{T,\text{water}} = \tfrac{1}{2}\rho_{\text{water}}U_{\text{water}}^2 A_{\text{parasitic}}\bar{C}_{D,\text{parasitic}}, \tag{8}$$

$$S_{\text{water}}\bar{C}_{T,\text{water}} = A_{\text{parasitic}}\bar{C}_{D,\text{parasitic}}, \tag{9}$$

where S_{water} is the wing planform area in water. Collecting terms and multiplying by $S_{\text{air}}\bar{C}_{z,\text{air}}$, we reach the following relation:

$$\frac{S_{\text{air}}\bar{C}_{z,\text{air}}}{S_{\text{water}}\bar{C}_{T,\text{water}}} = \frac{1}{k_{\text{parasitic}}}\frac{\bar{C}_{z,\text{air}}}{\bar{C}_{D,\text{air}}}. \tag{10}$$

Equation (10) definitively illustrates an aerial-aquatic compromise. The right-hand side includes the glide ratio $\bar{C}_{z,\text{air}}/\bar{C}_{D,\text{air}}$, which is usually designed to be much greater than 1 through the selection of a large wing aspect ratio. Furthermore, $k_{\text{parasitic}} < 1$ is the parasitic drag fraction, so $1/k_{\text{parasitic}}$ is also usually designed to be substantially greater than 1. Therefore, in order to ensure that the vehicle performance is not dominated by parasitic drag, the left-hand side of Eq. (10) must be even larger. In other words, a fit aerial-aquatic vehicle wants small parasitic drag (which necessitates an equally small underwater thrust), combined with large weight support (which necessitates a large aerial lift).

We now define the ratio between the aerial-aquatic force coefficients and wing areas as a scaling ratio C^*, which should be maximized to ensure good dual aerial-aquatic performance:

$$C^* = \frac{S_{\text{air}}\bar{C}_{z,\text{air}}}{S_{\text{water}}\bar{C}_{T,\text{water}}}. \tag{11}$$

The scaling ratio C^* as defined can obviously be made infinite by having zero underwater thrust $\bar{C}_{T,\text{water}} = 0$ and so must be restricted by the underwater self-propelled constraint of $A_{\text{parasitic}}\bar{C}_{D,\text{parasitic}} = S_{\text{water}}\bar{C}_{T,\text{water}}$ as the drag is never truly zero. For example, we can apply this analysis to the rhinoceros auklet data presented by Kikuchi *et al.* [37]: $m = 575$ g, $S_{\text{air}} = 0.043$ m^2, $S_{\text{water}} = 0.019$ m^2, $U_{\text{air}} = 15.3$ m/s, $U_{\text{water}} = 1.3$ m/s, and $A_{\text{fuselage}} \cong S_{\text{air}}$. Assuming a conservative fuselage drag coefficient of $C_{Df} = 0.01$ at Re $= 100\,000$ [35] and wrapping the wing profile drag into a net thrust coefficient rather than considering it a separate force, we obtain a very large scaling ratio $C^* \gg 1$:

$$\bar{C}_{T,\text{water}} = 0.023, \tag{12}$$

$$\bar{C}_{z,\text{air}} = 0.91, \tag{13}$$

$$C^* = 91. \tag{14}$$

As illustrated by Eq. (11), a high scaling ratio C^* can be achieved by substantially cutting the wing planform area underwater, cutting the force coefficients underwater, or both. The wing planform area does drop in auks by about a factor of 2 as they fold their wings while swimming [28,37,38]. However, morphing the wing area represents a difficult mechanical design problem for an engineered vehicle, especially given already ample complexity of high-degree-of-freedom wings. Controlling the force coefficients through the wing trajectory may be easier and can have a larger effect on C^*. Our goal, therefore, is to attempt the requisite change in force coefficients by only varying the wing trajectory. The lessons from this exercise are certainly applicable to area-changing wings, which would only enhance the effect.

Returning to Eq. (6), a similar Reynolds number in both air and water also hints at a plausible dynamic similarity argument between the two fluids. However, in order to achieve full dynamic similarity between air and water, the wing trajectory parameters must also be dynamically similar. This is not the case for real auks: The wing trajectory is very different between the fluids, given the different force requirements. Likewise, the final wing trajectories of a robotic solution would also be different between air and water.

However, we can certainly measure the force coefficients of a trajectory designed for air using an underwater test, taking advantage of full dynamic similarity. The Reynolds number, nondimensional frequency (Strouhal number St or reduced frequency k), wing geometry, stroke angle, and dihedral amplitude can all be exactly matched in an underwater experiment with an aerial motion trajectory. Given matching nondimensional parameters, the output force coefficients in air also match.

Aerial performance can therefore be predicted by measuring a dynamically similar aerial trajectory underwater. Aquatic performance, on the other hand, is predicted by directly measuring the aquatic trajectory underwater. This strategy is similar to that employed by Lock *et al.* [39]. As the experiments progress, we iteratively improve both types of trajectories though an optimization routine.

III. MATERIALS AND METHODS

The goal of our experiment is to elucidate the three-dimensional motion trajectories that would allow both enough lift for aerial weight support and the requisite thrust for underwater travel. Specifically, we postulate that, similar to aerial-aquatic animals, a variable stroke angle is the primary enabling factor that allows an engineered wing to reach the necessary force coefficients.

The specifications are derived as follows. First, we discuss the experiment apparatus and wing degrees of freedom (Sec. III A). Subsequently, we describe the wing's flapping parametrization (Sec. III B). The kinematics themselves are then optimized (Sec. III C) between subsequent experimental trials to maximize performance.

A. Experimental apparatus

We conduct our flapping-wing experiments underwater in the MIT Large Towing Tank, a 30 m long tank of cross section 2.5 m wide by 1.2 m deep. The apparatus itself is illustrated in Fig. 4(a). Our aerial-aquatic wing design requires explicit control over flapping motion, governing multiple degrees of freedom. As discussed in Sec. II A, two degrees of freedom, the dihedral motion and sweep motion, are necessary for manipulating the mean fluid force through the stroke angle. However, the wing must also pitch throughout the flapping cycle, thereby adding a third degree of freedom.

Unlike two-dimensional flapping, this pitch must vary over the wingspan in order to consistently maintain a reasonable angle of attack. During the wing motion, the flow at the root is parallel to the fuselage velocity U_{body}, meaning that ideally the root pitch is low in order to minimize the likelihood of stall. At the tip however, the wing has to pitch drastically, as the angle of the flow striking the wing tip can be extreme due to the motion of the wing.

The requirement for pitch twisting over the wingspan is often ignored in dihedral-only flapping experiments [11], but the effect in this paper is exaggerated by the forward-backward motion of the wing tip. For example, in the downstroke of the aquatic mode in Fig. 3, the wing tip must pitch down to nearly $-90°$ to avoid stall yet remain roughly zero near the root.

Maintaining low wing pitch at the root moreover complicates the mechanical implementation of an inclined stroke angle. An inclined stroke angle ($\beta \neq 90°$) can generally be achieved by one of two mechanisms.

(i) Fuselage pitch. Pitching the fuselage by some angle naturally adds forward-backward motion to the wing tip. Regrettably however, this also adds unwanted root pitch and increases the fuselage parasitic drag.

(ii) Dynamic wing sweep. Alternatively, time-varying wing sweep keeps both the wing root and fuselage level, but requires oscillating the wing sweep in addition to the dihedral.
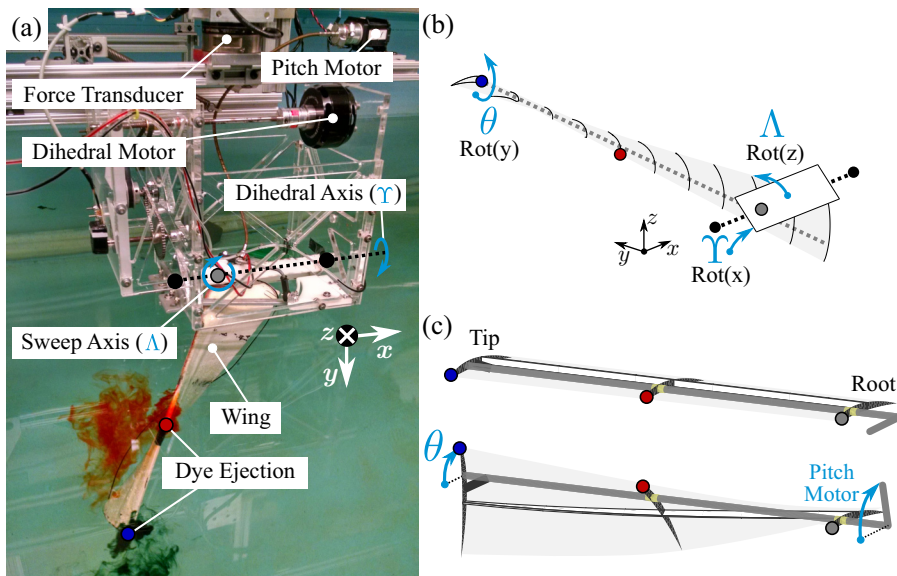
FIG. 4. Towing apparatus. (a) Photograph of flapping-wing apparatus in the MIT Towing Tank, with red and blue dye. (b) Definition of three Euler rotations: dihedral Υ, sweep Λ, and pitch θ. (c) Mechanism for pitching the wing tip and enforcing pitch along the wingspan.

Real birds, of course, do a combination of both [13], given redundant pitch and sweeps degrees of freedom at both the shoulder and wrist [40]. For the purposes of avoiding root stall, our experiment couples the wing sweep to the dihedral. Furthermore, the pitch is independently controlled, but is constrained to linearly vary from root to tip.

Accordingly, the wing moves in all three degrees of freedom illustrated in Fig. 4(b), controlled as follows.

(i) Dihedral Υ. The flapping dihedral motion is actuated by a rotary Tigermotor U11 motor, reduced by a 64:1 transmission ratio, and attached to the wing via a crankshaft (Appendix C). A rotary encoder logs the crankshaft position.

(ii) Sweep Λ. The wing sweep is coupled at various ratios to the dihedral using a tie rod, allowing arbitrary adjustment of the net stroke angle without affecting the root pitch. The mechanism is detailed in Appendix A (see also [41]).

(iii) Pitch θ. The wing pitch is actuated by an EX-106+ Dynamixel servomotor through a mechanism illustrated in Fig. 4(c). A rigid carbon-fiber spar at quarter chord pitches the wing tip, while the wing root stays at a fixed pitch throughout the motion. The pitch over the span is then rigidly enforced by a second stiff spar at half chord. This design is capable of achieving a wing-tip pitch of up to $\pm 100°$ and stroke angles of $45°$ to $135°$, all while maintaining zero pitch at the root.

In all tests the apparatus is tilted on its side with the wing dipped into the tank. Therefore, the standard global frame origin xyz for flight must also be tilted: x is downstream, y is along the wing's mean spanwise axis oriented towards the bottom of the tank, and z is lateral to the tank. Accordingly, the thrust force C_T is in the negative x direction and vertical flight force C_z is actually measured laterally during towing tests.

The wing itself is a rectangular-planform NACA6408 of aspect ratio $Æ\!R = 4$, chord length $c = 10$ cm, and span $R = 40$ cm. However, the free surface acts as a termination point for bound and shed vorticity [42], thereby increasing the effective aspect ratio, so the apparatus approximately mimics two root-flapping wings of total $Æ\!R = 8$. In all tests, the water surface is placed 5 cm below the wing root, as close as was possible to the flapping mechanism without submerging the apparatus and increasing the drag. All runs are performed at $U = 0.2$ m/s, corresponding to a chord Reynolds

TABLE I. Camera positions. Origin xyz is the wing root at the leading edge. The x axis is downstream, the y axis (along the wingspan) is mounted vertically in the tank with positive into the water, and z (normal to the wing) is lateral to the tank.

Camera	x (cm)	y (cm)	z (cm)
Left	10	24	−70
Right	15	24	67
Top	61	−81	3
Rear	113	24	6

number of $\mathrm{Re} = Uc/\nu = 20\,000$, somewhat lower than flying auks at $77\,000 \leqslant \mathrm{Re} \leqslant 102\,000$ [21] but in the same subcritical laminar regime of $10^3 < \mathrm{Re} < 10^6$ [43].

A six-axis ATI Gamma force transducer located above the apparatus measures all fluid forces and torques on the wing, logged with a 16-bit LTC1859 analog to digital converter simultaneously with the carriage position. Each run consists of eight flapping cycles after the carriage reaches steady velocity, of which the first two cycles are rejected to account for any additional startup transients. All data processing is performed in MATLAB. The force transducer signal before and after each run is subtracted from the measurement to remove transducer bias, steady buoyancy forces, and apparatus mass. Raw force data are filtered with a fifth-order Butterworth filter at eight times the flapping frequency, easily recording the dominant leading and trailing-edge vortex signals but rejecting signal from breakup of the foil's steady boundary layer. The inertial forces from accelerating the wing are simulated in postprocessing using Featherstone's Spatial_v2 MATLAB toolbox [44] and then subtracted out. After postprocessing, we obtain both instantaneous force coefficients $C_x(t)$, $C_y(t)$, $C_z(t)$, etc., from the fluid, as well as the mean forces $\bar{C}_x$, etc., over the flapping cycle.

Two dye-injection points are built into the wing to visualize the wake: blue dye at the wing tip and red dye at the midspan. The dye reservoirs are Mariotte's bottles, maintaining a constant pressure head regardless of reservoirs level. Four waterproof GoPro cameras with fisheye lenses record the wing and dye motion: one on each side of wing, one downstream, and a final camera above the water surface. Exact placements are listed in Table I. A flash bulb triggered by the logging software synchronizes the dye visualization cameras with each other, the force data, and the kinematic data.

B. Flapping motion parametrization

The parameter space for flapping flight is huge, especially in natural biological systems. For the engineering implementation, we have limited the apparatus to dihedral amplitude of $\pm 45^\circ$ and stroke angles $45^\circ \leqslant \beta \leqslant 135^\circ$. The wing pitch linearly increases from root to tip.

The flapping frequency $f = (2\pi)^{-1}\omega$ of wings is usually nondimensionalized as a Strouhal number $\mathrm{St} = fA/U$, where A is the wake width. As the wake width itself is difficult to determine a priori, a variety of definitions for width A have been used throughout the flapping flight literature that instead substitute some type of motion amplitude. For example, Taylor $et\ al.$ [4] use the vertical excursion of the wing tip, while Techet [9] uses the arc length of excursion of a point inboard of the wing tip. We use the arc length of the $\pm 45^\circ$ wing-tip dihedral motion, as the wing is highly tip loaded, for the convenient expression

$$\mathrm{St} \equiv \frac{R\pi}{2} \frac{f}{U}, \tag{15}$$

where R is the wing semispan. We fix the Strouhal number at $\mathrm{St} = 0.4$, as it is within the range reported in natural examples of flapping flight $0.2 \leqslant \mathrm{St} \leqslant 0.4$ [4], while still high enough to allow for full use of the variable stroke angle [18]. If the flapping frequency is too low, the stroke angle has only little effect as the freestream dominates the oncoming flow angle. At this Strouhal number, the wing geometry and flow speed fix the flapping period T at 8 s.

Three Euler angles of the wing (dihedral, sweep, and pitch) give a rotation matrix $\mathbf{R}_w^g$ for the wing normal vector in the body frame $\mathbf{n}^b$ to the global frame $\mathbf{n}^g$,

$$\mathbf{n}^g = \mathbf{R}_b^g \mathbf{n}^b, \tag{16}$$

$$\mathbf{R}_b^g = \mathbf{R}_x(\Upsilon)\mathbf{R}_z(\Lambda)\mathbf{R}_y(\theta). \tag{17}$$

Throughout the paper, the dihedral $\Upsilon(t)$ is defined as positive with wing tips up, the pitch $\theta(s,t)$ is positive nose up, and the sweep $\Lambda(t)$ is positive wing tips forward, corresponding to positive x, y, and z rotations for the right wing, respectively, again illustrated in Fig. 4(b). The distance s is the spanwise coordinate from the wing root to the point of interest.

The sweep and dihedral are coupled together to obtain motion in a single plane (Appendix A), tilted from the horizontal by the stroke angle β:

$$\Lambda(t) = -\arctan[\cot\beta \sin\Upsilon]. \tag{18}$$

Finally, the wing pitch $\theta(s,t)$ is mechanically constrained to be linear pitch from root to tip,

$$\theta(s,t) = \theta(R,t)\frac{s}{R}, \tag{19}$$

and the wing-tip geometric angle of attack can be determined by subtracting the incident flow angle $\theta_{\text{flow}}(R,t)$ (Appendix B) computed from the freestream and wing motion

$$\alpha(R,t) = \theta(R,t) - \theta_{\text{flow}}(R,t). \tag{20}$$

In summary, the combination of one parameter and one continuous-time variable determines a baseline wing motion: the stroke angle β and the wing-tip pitch $\theta(R,t)$ [or wing-tip geometric angle of attack $\alpha(R,t)$]. The Strouhal number and Reynolds number are fixed at St $= 0.4$ and Re $= 20\,000$, respectively, and the dihedral amplitude of max$[\Upsilon(t)] = 45°$. All degrees of freedom, the dihedral $\Upsilon(t)$, sweep $\Lambda(t)$, and wing-tip pitch along the span $\theta(s,t)$, can be subsequently derived.

C. Trajectory selection and feedback

Determining an ideal wing-tip pitch $\theta(R,t)$ is still nontrivial, as the geometric wing-tip angle of attack $\alpha(R,t)$ is not necessarily predictive of the force in unsteady flapping flight. This geometric angle of attack measures the angle between the wing and its motion, not between the wing and the fluid. The wake will create induced flows that disturb the quiescent inflow, altering the true angle of attack and therefore the fluid force. Trajectory modifications are needed to ideally determine the motion to achieve any desired force profile.

We therefore use an optimization routine to determine trajectories for aerial and aquatic motions. The steps, explained in more detail in the following sections, can be summarized as follows.

Step 1. Determine an initial guess for kinematics of the wing pitch, for any given stroke angle and peak angle of attack.

Step 2. Determine a desired force profile for the given stroke angle and peak angle of attack.

Step 3. Perform an experiment-based optimization: (a) Run the kinematics through the experiment, measuring the fluid force through the force transducer, (b) compare the experiment-measured force to the desired force and determine corrections to the kinematics, and (c) repeat Step 3 until converged.

1. Initial kinematics

As a first-attempt initial wing kinematics prior to optimization, we employ the Theodorsen effective [45] angle of attack. The effective geometric angle of attack of a pitching cambered wing is taken at the three-quarter chord rather than the quarter chord,

$$\alpha_{3/4}(R,t) = \alpha(R,t) - \alpha_{C_L=0} + \frac{\dot{\theta}(R,t)c}{2\|V(R,t)\|}, \tag{21}$$

where the $\dot{\theta}$ term accounts for lift due to pitch rate and V is the flow speed perpendicular to the span (Appendix B). While this effective geometric angle of attack still does not include the wake effects, we can impose a functional form on $\alpha_{3/4}$ with reasonable confidence that the wing force measured from the force transducer will follow a similar form. Accordingly, we use a piecewise $\alpha_{3/4}$ that peaks in the middle of the downstroke and is zero throughout the upstroke,

$$\alpha_{3/4}(R,t) = \begin{cases} \alpha_{\max} \times \{0.5 - 0.5\cos[2\phi(t)]\} & 0 \leqq \phi(t) < \pi \\ 0 & \pi \leqq \phi(t) < 2\pi, \end{cases} \tag{22}$$

where $\phi(t)$ is the flapping phase of the dihedral varying from 0 to 2π over the flapping cycle. Equation (22) makes an effective angle of attack during the downstroke $[0 \leqslant \phi(t) < \pi]$, peaking at $\alpha_{\max}$ at the middle of the downstroke $[\phi(t) = \pi/2]$, and then has a zero angle of attack throughout the upstroke $[\pi \leqq \phi(t) < 2\pi]$. The initial pitch kinematics of the wing tip $\theta(R,t)$ can then be quickly determined by ordinary differential equation (ODE) methods to simultaneously solve Eq. (21) at $s = R$ for both θ and $\dot{\theta}$ at the wing tip [19]:

$$\dot{\theta}(R,t) = \frac{2\|V(R,t)\|}{c}\Big[\alpha_{3/4}(R,t) + \alpha_{C_L=0} + \theta_{\text{flow}}(R,t) - \theta(R,t)\Big]. \tag{23}$$

2. Desired force profile

To obtain a desired force profile as a target for the optimization, we must limit our selection to forces that are achievable by the wing. Accordingly, we use a predictive reduced-order model described by Izraelevitz *et al.* [46] to bound this selection. We run this model only on the first initial trajectory, prior to running any experiments, to create a desired force profile that each subsequent experiment trail is compared against.

Rather than a full representation of the wake, this fast reduced-order model for flapping flight employs $O(n) = 10$ states to represent the dynamics between the wing angle of attack, circulation, and lift force. The model has been validated against both vortex lattice methods and the experiments of Scherer [47]. Large-amplitude wing motion, added mass, three-dimensional (3D) tip effects, dynamic wing circulation, and trailing-edge vortex shedding are all included. To account for viscous effects, we additionally include a conservative 2D profile drag $C_D(\alpha) = 0.1 + \alpha^2$ and unstalled high angle-of-attack lift $C_L(\alpha) = 2\pi \sin\alpha \cos\alpha$ [43] on top of the inviscid model. However, as the model does not account for all wake effects, including leading-edge shedding, stall, and wake roll-up, there is still adequate room for the experiment-based feedback.

3. Discrete control between experiment trials

Of course, the measured force from the experiment will naturally include additional unwanted forces, due to wake effects changing the true oncoming flow direction. However, these unmodeled forces are easily corrected by slight adjustments to the kinematics [18]. By taking the difference between the desired and measured force, we can develop a learning cycle between experiment trials to incrementally improve the pitch trajectory of the wing tip $\theta(R,t)$.

First, we hypothesize that the wing-tip loading is high due to the large velocity at the wing tip. Therefore, the wing-tip angle of attack makes a reasonable selection for the control input. Second, we assume that only motion-relative lift C_L is controllable:

$$C_L(t) = \frac{2\mathbf{F}(t)}{\rho U^2 S} \begin{bmatrix} \sin[\theta_{\text{flow}}(R,t)] \\ 0 \\ \cos[\theta_{\text{flow}}(R,t)] \end{bmatrix}. \tag{24}$$

This force C_L is oriented normal to the motion direction, rather than always in the z direction. After obtaining both a desired force and the experiment force measurement, we take the difference between
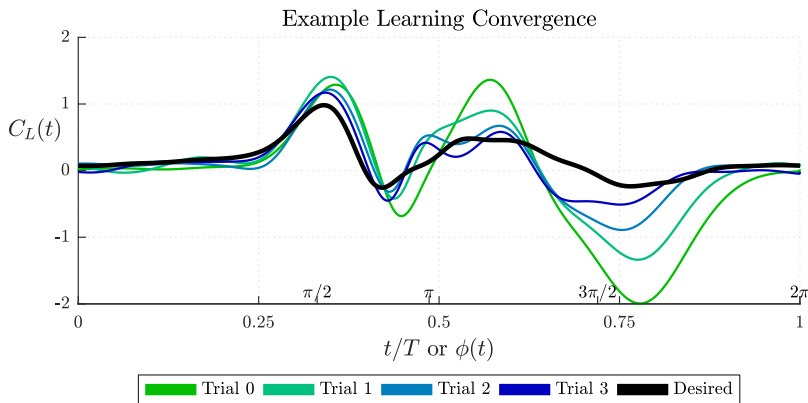
FIG. 5. Optimization routine example. Aquatic trajectory (St $= 0.4$, $\beta = 135°$, and $\alpha_{\max} = 15°$) after successive experimental trials, driving down the error between the desired motion-relative lift (black) and experimental motion-relative lift.

$C_{L,\text{desired}}(t)$ and $C_{L,\text{experiment}}(t)$ to provide an error signal $e(t)$,

$$e(t) = C_{L,\text{desired}}(t) - C_{L,\text{experiment}}(t). \tag{25}$$

This error is translated into a change in the wing tip α_{eff} by inverting the quasisteady lift formulation

$$\Delta\alpha_{\text{eff}}(t) = \frac{e(t)}{2\pi S_{\text{eff}}^* V(t)^2/U^2}, \tag{26}$$

where S_{eff}^* is a nondimensional gain (effective normalized wing area) between the expected force due to changing the wing-tip angle of attack versus pitching the entire wing. From the model results, we can fit the gain $S_{\text{eff}}^* \approx 1/6$, combining both the Wagner effect [48] for decreased unsteady lift and the high-wing-tip loading compared to the rest of the wing.

Finally, we add a learning rate $0 \leqslant k \leqslant 1$ to avoid overshoot during the optimization. The force from each experiment trial angle of attack α_{eff}^n informs the corrections $\Delta\alpha_{\text{eff}}^{n,n+1}$ needed to perform the next trial $\alpha_{\text{eff}}^{n+1}$:

$$\alpha_{\text{eff}}^{n+1}(t) = \alpha_{\text{eff}}^n(t) + k\Delta\alpha_{\text{eff}}^{n,n+1}(t). \tag{27}$$

The new pitch trajectory of the wing tip $\theta^{n+1}(R,t)$ is then determined through solving Eq. (23) with the new effective angle of attack $\alpha_{\text{eff}}^{n+1}(t)$.

Our optimization routine, effectively a discrete controller designed through feedback linearization, slowly modifies the wing-tip pitch trajectory (and thereby the linear pitch on the entire wing span) so that the experimentally measured lift matches the desired lift of the original motion. This allows us to preserve both the low force oscillation of an inactive upstroke and the desired wide envelope C^*, even if the open-loop flapping results from the initial pitch trajectory are unsatisfactory.

Figure 5 illustrates one such optimization in progress. The iterations are colored from light green to dark blue, with the desired force in black. Each iteration lowers the error between the desired force and experiment, with the root-mean-square error dropping from 0.7 to 0.2.

IV. RESULTS

The experiment results for all tested trajectories, through all optimization steps, are illustrated in Fig. 6. In total, we optimized nine trajectories (three β by three $\alpha_{\max}$ at fixed St $= 0.4$) and ran each optimization for three iterations at a learning rate of $k = 0.5$.

For each trajectory, Fig. 6 gives the mean horizontal force in x, vertical force in z, and a Lissajous curve [$C_x(t)$ vs $C_z(t)$] of the instantaneous force over the flapping cycle. Similar to the color scale
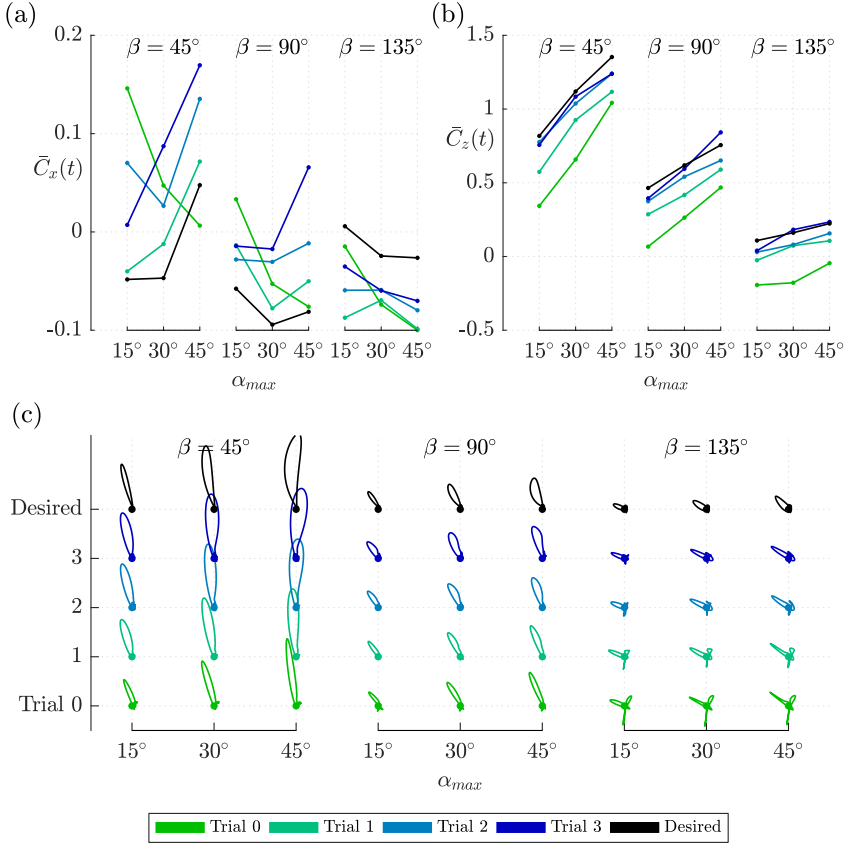
FIG. 6. Experiment trajectory optimization. (a) Mean horizontal force for each trial of each trajectory. (b) Mean vertical force for each trial of each trajectory. (c) Force direction Lissajous curves over the course of the flapping cycle.

in Fig. 5, the desired performance is in black, open loop trajectories are in green, and the converged trajectory is in blue. Results are phase averaged over six flapping cycles.

In general, the optimization inactivates the upstroke, thereby increasing the net vertical force $\bar{C}_z$ in Fig. 6(b) and decreasing the net thrust $\bar{C}_T$ (i.e., increasing $\bar{C}_x$) in Fig. 6(a). As the motion-relative lift is generally more aligned with the z axis than with the x axis, $\bar{C}_z$ converges over the course of the experiment trials.

Note that in the trial-0 open-loop results of Fig. 6(c), there is a strong oscillatory force component especially for the larger stroke angles. For these trajectories, the Lissajous curves are messy, indicating a time-varying force direction. As expected, the initial pitch definition does not necessarily perform well in the experiment. However, after the optimization, the Lissajous curves in Fig. 6(c) have only one large petal due to the active downstroke (see trial 3, in blue).

Furthermore, the wide range in mean force coefficients $\bar{C}_x$ and $\bar{C}_z$ is consistent with the scaling ratio C^* required for aerial-aquatic operation. For example, the measured force from this selection already overlaps the force envelope of rhinoceros auklets discussed in Eq. (14), i.e., $\bar{C}_{T,\text{water}} = 0.023$ and $\bar{C}_{z,\text{air}} = 0.91$.

A detailed look at a few of these trajectory cases, with wake visualization, is given in the following sections. The trajectories, all with a loaded downstroke and an unloaded upstroke at St $= 0.4$, are

(i) a low-thrust aquatic trajectory at a tilted stroke angle of $\beta = 135°$, with $\alpha_{\max} = 15°$, the same as the example trajectory in Fig. 5,
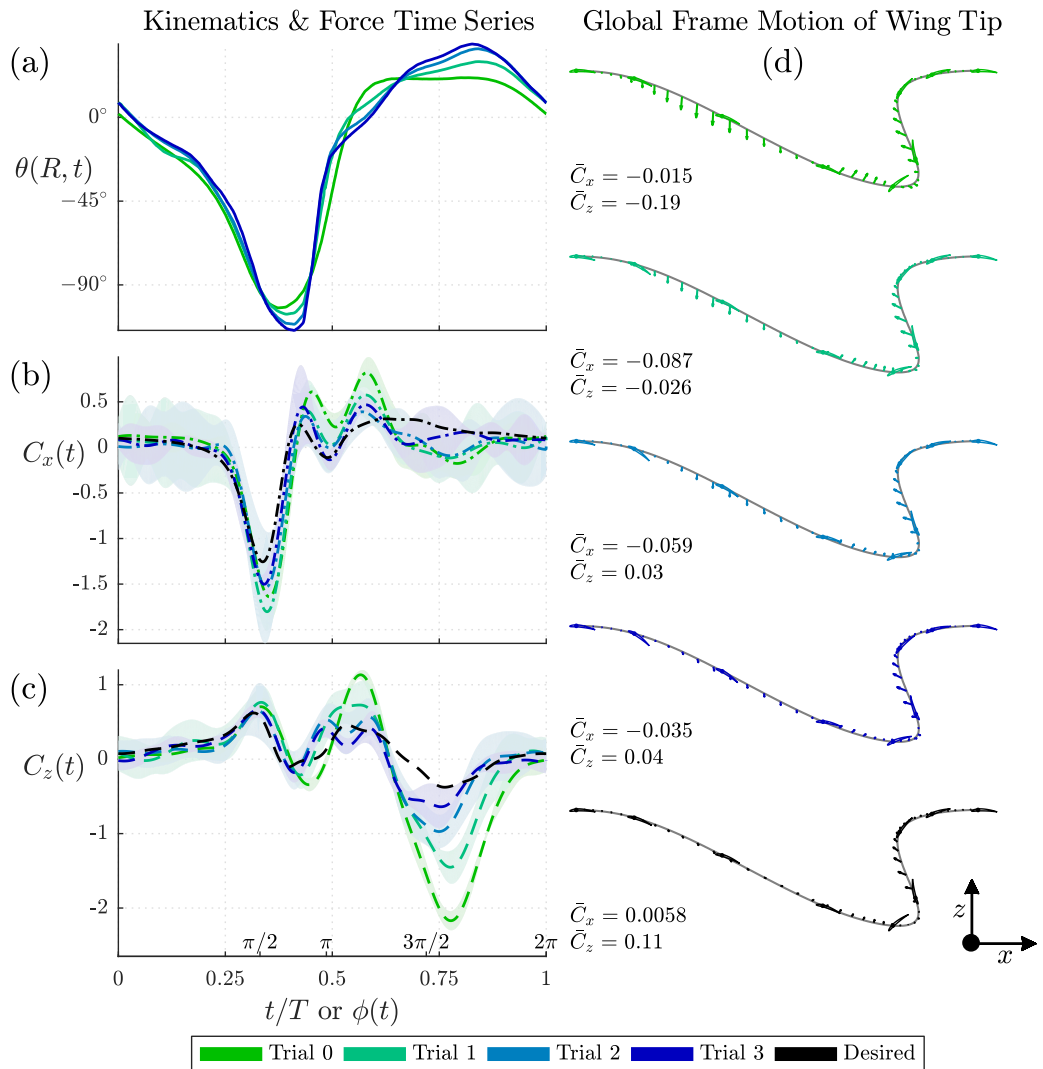
FIG. 7. Aquatic motion trajectory. Experiments of a trajectory employing a backward-moving downstroke (stroke angle $\beta = 135°$), maximum angle of attack $\alpha_{\max} = 15°$, and flapping frequency given by St $= 0.4$ are shown for the (a) trajectory of the wing-tip pitch $\theta(R, t)$, (b) thrust coefficient (envelopes on each curve indicate two standard deviations over six runs), (c) vertical force coefficient, and (d) global motion of the wing tip, with superimposed wing-tip orientation and instantaneous total force.

(ii) a boosted lift aerial trajectory at a tilted stroke angle of $\beta = 45°$, with $\alpha_{\max} = 45°$, and
(iii) a baseline dihedral-only trajectory of $\beta = 90°$, with $\alpha_{\max} = 45°$.

A. Aquatic trajectory for low thrust ($\beta = 135°$ and $\alpha_{\max} = 15°$)

A trajectory designed for aquatic travel is illustrated in Fig. 7. The goals for this trajectory are twofold: (1) a small net thrust $\bar{C}_x \leqslant 0.05$ from the oversized wing to counteract the fuselage drag and (2) for that force to stay unidirectional with an inactive upstroke to reduce the risk of destabilizing the vehicle.

Figure 7 summarizes the effectiveness of each iteration of the optimization. Over the course of the optimization, the kinematics and force, represented in Fig. 7(a) and Figs. 7(b) and 7(c), respectively, change as the routine attempts to recreate the intended performance. Figure 7(d) gives a visual summary of the different trajectories, simultaneously showing the total vectorial force and wing-tip motion.

Initially, the kinematics $\theta(R,t)$ are derived from the effective angle of attack $\alpha_{\text{eff}}(R,t)$ profile in Eq. (22). However, this motion does not have a unloaded upstroke. The initial experiment contains a slight force peak to $C_z(t) = 1$ at the beginning of the upstroke [$\phi(t) \cong \pi$], followed by an unwanted $C_z(t) = -2$ during the middle of the upstroke [$\phi(t) \cong 3\pi/2$]. The desired force includes no such upstroke force, and given that the intended force direction is in x, the oscillating forces in z are parasitic.

These oscillatory forces result from unmodeled effects in the initial motion parametrization. Given a tilted stroke angle of $\beta = 135°$, the velocity of the wing tip in this trajectory is highest during the upstroke, precisely when we want zero force. The velocity mismatch amplifies the effect of small-angle-of-attack errors. The true angle of attack (averaged over the span) is slightly negative during the upstroke due to an effect not captured by the model, such as possibly overcorrecting for the expected rotation-induced lift at the beginning of the upstroke.

Fortunately, the oscillations in $C_z(t)$ are easily minimized through the use of feedback. After three iterations through the optimization routine, the C_z forces stay small throughout the flapping cycle. Furthermore, the mean thrust after optimization is slightly increased so that it is of the intended magnitude of expected fuselage drag. The mean thrust coefficient $\bar{C}_T = -\bar{C}_x = 0.035$ is comparable to the drag coefficient of a streamlined underwater vehicle at $\text{Re} = 20\,000$ and the required thrust calculated by Kikuchi *et al.* [37] [Eq. (14)]. The thrust coefficient can also be increased if needed by including an active upstroke, at the cost of an oscillating vertical force.

Figure 8 gives a qualitative dye visualization of the trajectory's 3D wake. Three camera feeds (top, left, and rear) capture the streaklines from the leading edge of the midwing (red) and wing tip (blue). As standard in dye visualization, all dye is not necessarily vorticity and not all vorticity will be captured depending on the location of the dye lines. Dye originating from the wing's leading edge highlights leading-edge vortices (LEVs), especially since the spanwise flow in the LEV core will spread the dye if the LEV remains attached. The blue dye at the wing tip furthermore will accent wing-tip vortices (WTVs). However, trailing-edge vortices (TEVs) are harder to see with this technique, especially from viewing angles normal to the core line, as the dye does not have as much time to spread spanwise as a free vortex.

From the top camera view, both the LEV and TEV are visible. These vortices roll up and convect faster than the freestream flow [Fig. 8(c) at $3\pi/4 \leqslant \phi \leqslant 5\pi/4$, top camera]. The rear and left cameras give a more detailed view of the geometry of the LEV and WTV, but the starting TEV is less distinct from this viewpoint.

In total, dye visualization shows a coherent vortex ring shed during the downstroke [Fig. 8(b)]. This vortex ring consists of the starting and stopping vortices of the midwing (TEV and LEV respectively) and the WTV linking them together. The vorticity distribution is a highly twisted version of the classic scheme described by Rayner [49]: A single vortex ring shed every downstroke, followed by only shear breakup each upstroke.

Near the wing tip, the jet bounded by this vortex ring faces downstream, consistent with the thrust measured by the force transducer. The ring geometry is a three-dimensional variant of two-dimensional pulsed jet wake described by Izraelevitz and Triantafyllou [18] at a $\beta = 135°$ stroke angle. Similar to two dimensions, roughly aligning the TEV and LEV along the z axis generates thrust along the x axis, but unlike two dimensions, the wing must include a variable pitch over the span to align appropriately with the motion-induced flow and the vortex ring is necessarily highly twisted.

Beyond the vortex structures, the dye visualization also gives a tangible illustration of the control action. Figure 9 shows the pressure side of the wing (left camera) before and after the optimization during the trajectory upstroke. Note the pooling dye on the open-loop trajectory at the
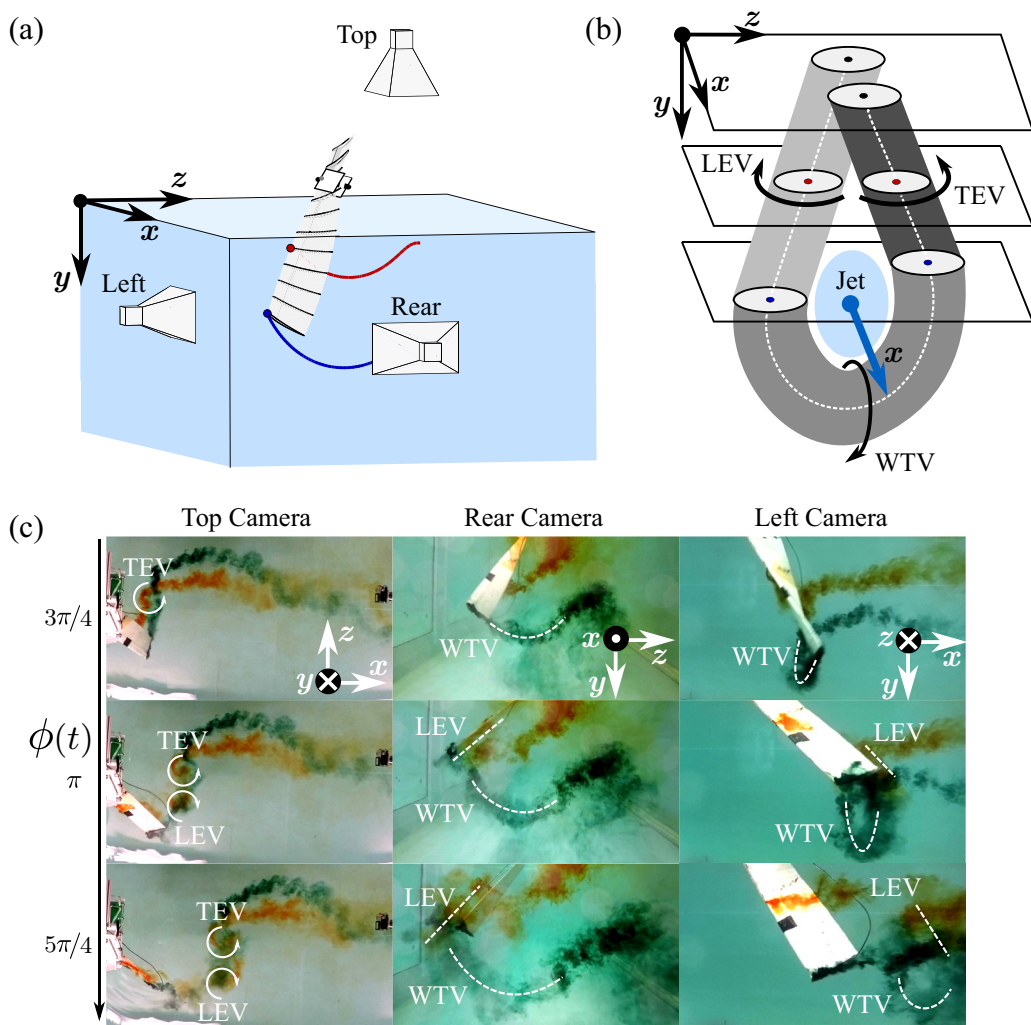
FIG. 8. Aquatic motion dye visualization. (a) Cartoon of camera placements around the wing (not represented at scale). (b) Diagram of visualized wake, consisting of a twisted vortex ring with central jet. (c) Snapshots from the top, rear, and left cameras of the trajectory at the transition between the downstroke and upstroke ($\phi = 3\pi/4$ to $\phi = 5\pi/4$). The leading-edge vortex (LEV), trailing-edge vortex (TEV), and wing-tip vortex (WTV) are labeled wherever distinct. Flow is in the positive x direction. All images have been enhanced in both lightness and contrast by 10% for clarity.

end of the upstroke [$\phi(t) = 7\pi/4$ and $\phi(t) = 2\pi$], indicating separated regions that are removed by manipulating the angle of attack. In swimming auks, such wing pitch control is certainly achievable due to the active degrees of freedom in the avian wrist or perhaps even passively by relaxing muscles at appropriate times.

B. Aerial trajectory for boosted lift ($\beta = 45°$ and $\alpha_{max} = 45°$)

Next, Fig. 10 illustrates an aerial trajectory with a forward-moving downstroke. This trajectory is designed to increase the available vertical force, mimicking the requirements of flying auks. As
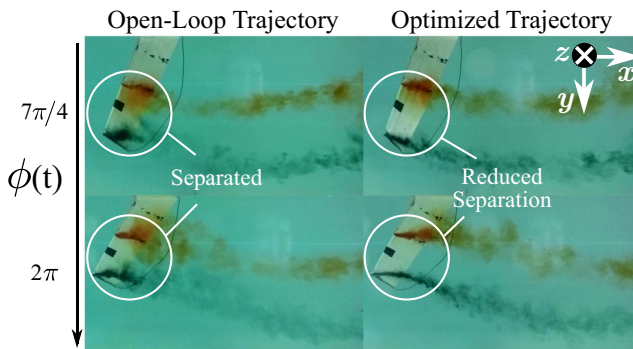
FIG. 9. Dye visualization of control action. Comparison of the open-loop trajectory to the optimized trajectory after three iterations. Snapshots are from the left camera (wing pressure side), near the end of the upstroke ($\phi = 7\pi/4$ and $\phi = 2\pi$). All images have been enhanced in both lightness and contrast by 10% for clarity.

discussed by Pennycuick [21], auks in flight have smaller wingspans than other of the same mass and must therefore compensate with larger vertical force coefficients to offset the body mass.

Unlike the aquatic case (Sec. IV A), the optimization is not strictly required to isolate the force only to the downstroke, as the open loop kinematics already do a reasonable job. However, the optimization does converge the vertical force $C_z(t)$ towards the desired force. Again, the drag at the beginning of the downstroke is uncontrolled by the routine, so C_x increases over the course of the learning.

True to the promises of using a variable stroke angle, the vertical force is tremendously boosted. In fact, the vertical force coefficient peaks to $C_z(t) = 8$ in the middle of the downstroke in Fig. 10(c), over five times the maximum force of the aquatic trajectory. Furthermore, the coefficient from the experiment now matches the aerial requirements $\bar{C}_z \geqslant 0.96$ listed in Sec. II B. With respect to the baseline trajectory without sweep motion ($\bar{C}_z = 0.84$; see the next section), the mean coefficient $\bar{C}_z = 1.2$ is also an improvement.

Figure 11 shows the dye visualization of this aerial high-force trajectory. Similar to the aquatic trajectory, the LEV and TEV are visible from the top view, while LEV and WTV are visible from the side and rear views. For this trajectory, we use the right camera rather than the left to better highlight the attached downstroke LEV and so must represent the freestream mirrored from the usual standard.

By the second half of the downstroke ($\phi = 3\pi/4$), an attached LEV appears well developed and the trailing-edge vorticity begins to wrap into a coherent TEV [Fig. 11(c)]. The LEV remains attached until the end of the downstroke ($\phi = \pi$), which is most easily seen from the right views. As the wing is moving quickly upstream during the downstroke, the dye is weaker and more spread out. However, we can still see the faint signs of the LEV once it is shed into the wake. The WTV, clearly swirling in the rear views, links the trailing-edge vorticity to the shed LEV. Again, this wake structure is analogous to the two-dimensional high-lift trajectories discussed by Izraelevitz and Triantafyllou [18], where upstream wing motion increases the force magnitude and orients its direction to be transverse to the flow.

C. Baseline dihedral-only trajectory ($\beta = 90°$ and $\alpha_{\max} = 45°$)

Finally, we discuss a trajectory with constant sweep $\Lambda(t) = 0$ with only the dihedral flapping motion active (i.e., $\beta = 90°$). Again, the root pitch remains at zero, while the wing pitches linearly along the span to the wing tip. We choose the maximum wing-tip effective angle of attack $\alpha_{\max} = 45°$ to attempt to generate as much lift as possible with this motion, simulating slow aerial flight if a variable stroke angle is not possible.
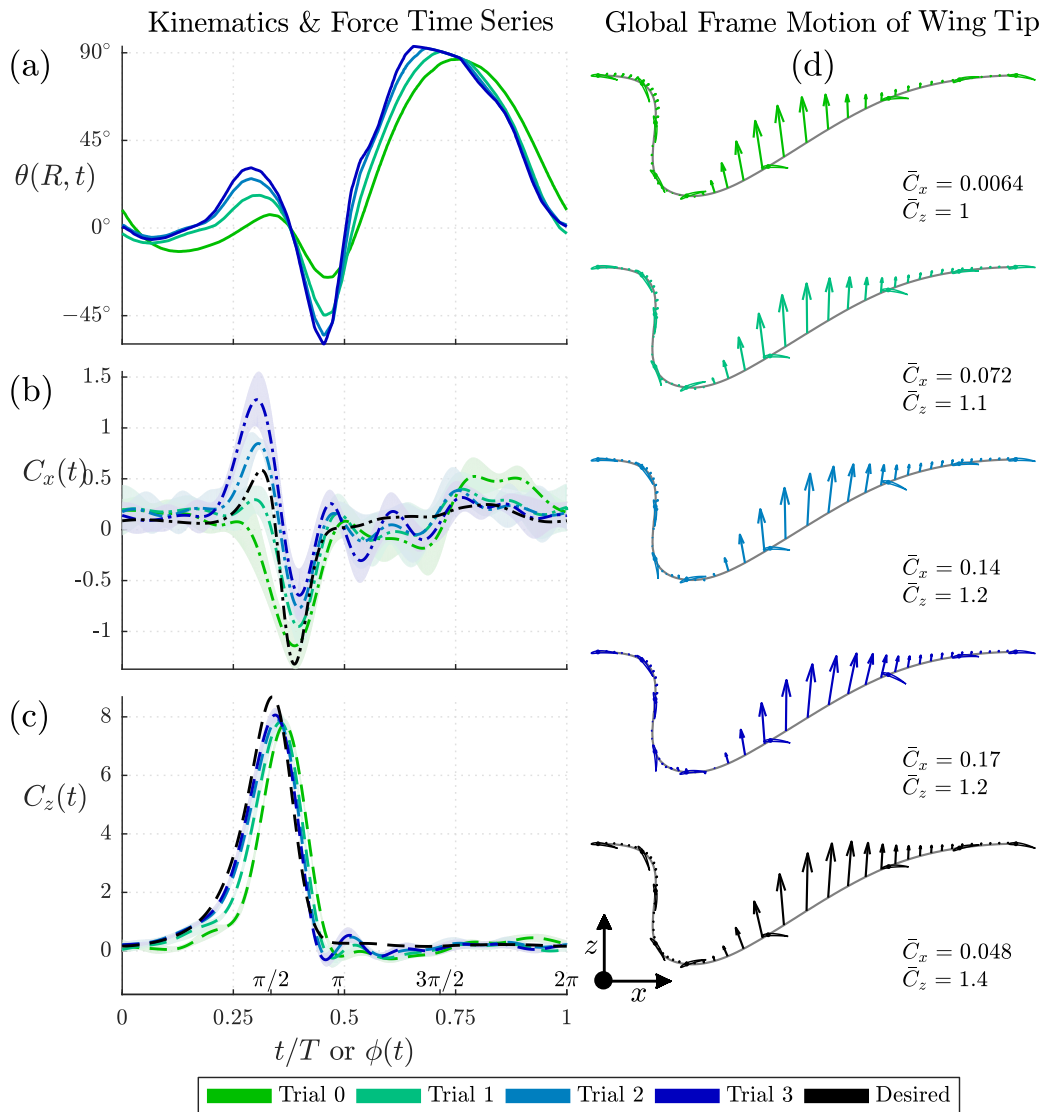
FIG. 10. Aerial motion trajectory. Experiments of a trajectory employing a forward-moving downstroke (stroke angle of $\beta = 45°$), maximum angle of attack $\alpha_{\mathrm{max}} = 45°$, and flapping frequency given by St = 0.4 are shown for the (a) trajectory of the wing-tip pitch $\theta(R,t)$, (b) thrust coefficient (envelopes on each curve indicate two standard deviations over six runs), (c) vertical force coefficient, and (d) global motion of the wing tip, with superimposed wing-tip orientation and instantaneous total force.

Similar to the aerial case with dynamic sweep (Sec. IV B), the model predicts the performance reasonably well and the optimization converges the lift magnitude [Fig. 12(c)]. In open loop, the wing force is already largely isolated to the downstroke, where the force peaks to $C_z = 3.5$ and $C_x = -1.5$. The optimization scheme only tries to control the lift perpendicular to the motion of the wing tip $\theta_{\mathrm{flow}}(s,t)$, hence the drag $C_x(t)$ is uncontrollable whenever $\theta_{\mathrm{flow}}(s,t) \approx 0$. We therefore do not expect convergence of $C_x(t)$ near the beginning or end of the downstroke $\phi(t) = 0$ and $\phi(t) = \pi$ in Fig. 12(b), but after optimization the rest of the trajectory suitably matches the desired force.
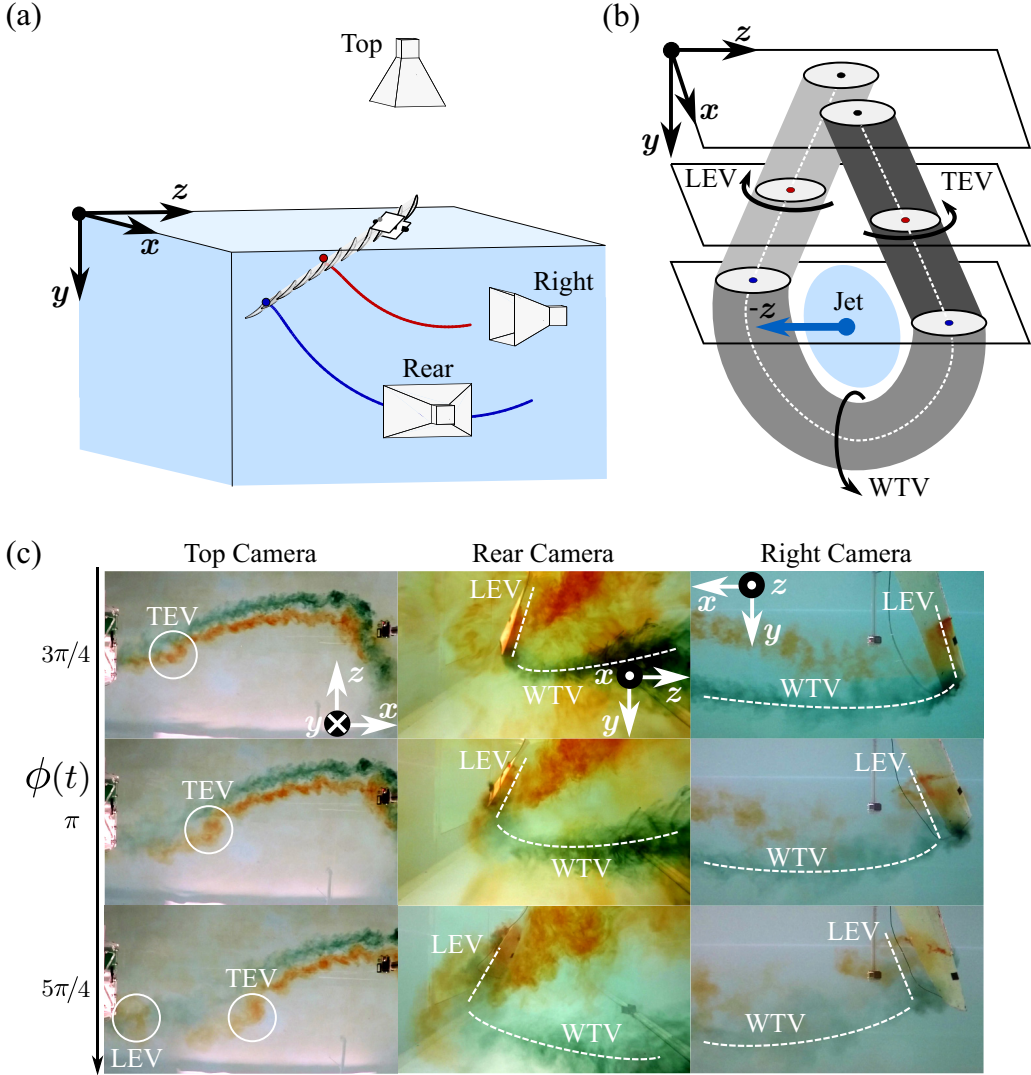
FIG. 11. Aerial motion dye visualization. (a) Camera placements for aerial motion. (b) Wake diagram, now with a z-oriented jet. (c) Snapshots of dye visualization. Similar to Fig. 8, flow is again in the positive x direction and all images have been enhanced in both lightness and contrast by 10% for clarity.

V. CONCLUSION

In summary, an active stroke angle increases the force envelope of a flapping wing, as compared to a rigid stroke angle at $90°$. For aerial motions, the wing moves upstream during the power stroke, boosting the instantaneous velocity of the wing tip and thereby the vertical force. For aquatic motions, the wing moves downstream during the power stroke, tilting the flow direction so that the force is mostly thrust aligned with the x axis. A further necessary condition for this force control is an angle-of-attack asymmetry, where the downstroke has an intentionally larger force than the upstroke.

We demonstrate this force envelope using an experimental wing of three degrees of freedom: dihedral (up-down) flapping, dynamic wing sweep (forward-backward), and wing pitch. The pitch distribution along the wingspan allows the wing tip to pitch drastically to follow the wing-relative flow, while still keeping the root angle of attack small to avoid root stall.
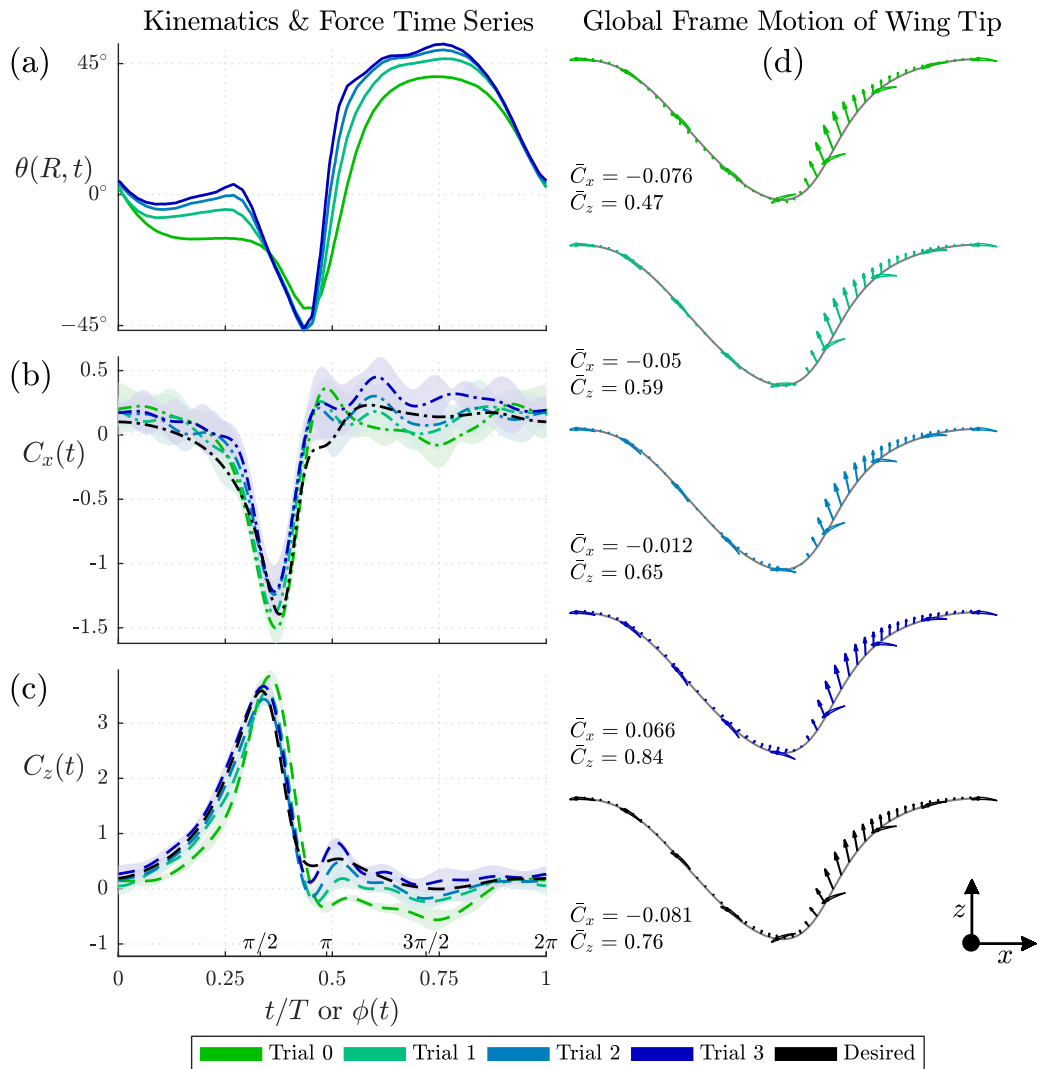
FIG. 12. Dihedral-only trajectory. Experiments of an unswept wing employing only a dihedral motion (stroke angle $\beta = 90°$), maximum angle of attack $\alpha_{\max} = 45°$, and flapping frequency given by St $= 0.4$ are shown for the (a) trajectory of the wing-tip pitch $\theta(R,t)$, (b) thrust coefficient (envelopes on each curve indicate two standard deviations over six runs), (c) vertical force coefficient, and (d) global motion of the wing tip, with superimposed wing-tip orientation and instantaneous wing force.

Using learning to automatically modify the trajectories between experimental trials dramatically improves the performance of the wing. Our chosen algorithm uses discrete feedback linearization between successive force transducer measurements to guide the force time series. The algorithm both removes unwanted variation of the forces during the time series and converges selected mean force coefficients towards desired values.

Furthermore, we present flow visualizations that demonstrate the presence of coherent wake vortex structures. The visualized wakes are a twisted form of the TEV-WTV-LEV linkup. At the beginning of the downstroke, the wing sheds a TEV, signaling bound circulation on the wing. This bound circulation then separates as a LEV, and the WTV links the LEV and TEV together as a finite-span effect. In thrust-generating wakes, the TEV and LEV are placed as boundaries of a streamwise jet,

while the vortices bound a wide vertical jet in lift-producing trajectories. These vortex structures are reminiscent of the two-dimensional wakes at variable stroke angle discussed by Izraelevitz and Triantafyllou [18], with the addition of a WTV and twisted geometry. The flow visualization moreover confirms the method of control action; the feedback reduces flow separation and appropriately orients the wake to provide force in the correct direction.

Finally, the force illustrated from this experiment covers the expected coefficient range needed to enable dual aerial-aquatic flight. When implementing this on a dual aerial-aquatic vehicle, the wing planform area does not necessarily need to vary between the two fluids; a variable trajectory can be sufficient to match the desired force coefficients. This phenomena matches observations from biology, where wing-propelled dual flying and swimming birds are known to analogously vary their wing motion to compensate for the change in fluid properties between air and water.

APPENDIX A: STROKE ANGLE MECHANISM

Rather than pitch the entire apparatus to change the stroke angle, the wing forward-backward motion is instead implemented by a dynamic wing sweep. The sweep and dihedral are coupled by a tie-rod mechanism (Fig. 13).

As the dihedral motor rotates a crankshaft, it oscillates a stiff auxiliary structure about the dihedral-axis bearings. A second set of bearings at the wing root then adds a sweep degree of freedom between the wing and the auxiliary structure. The sweep motion and dihedral motion are coupled by a tie rod.
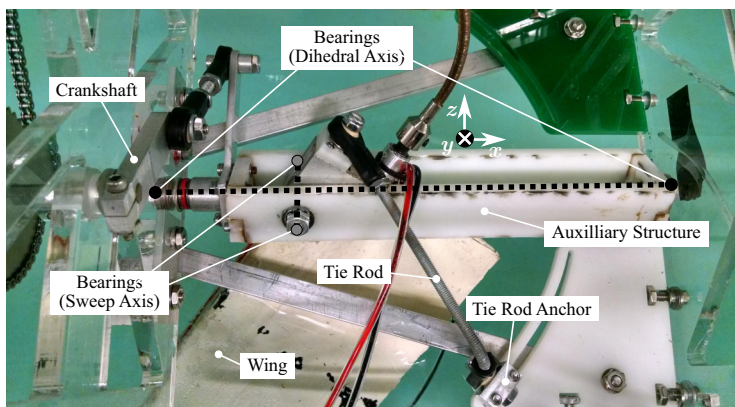

FIG. 13. Stroke angle mechanism. Photograph of setup for constraining the dihedral and sweep motions to follow a tilted stroke angle.

This tie rod adds the constraint that one point on the wing must always remain a fixed distance to the tie rod anchor, thereby enforcing a flapping axis coincident to the wing root and tie-rod anchor. The stroke angle is then adjusted manually by moving the location of the tie-rod anchor along a circular slot.

To determine the net motion of this mechanism, we equate the rotations in the sweep $\mathbf{R}_z(\Lambda)$ and dihedral $\mathbf{R}_x(\Upsilon)$ to equivalent rotations about the inclined stroke axis

$$\mathbf{R}_y(90° - \beta)\mathbf{R}_x(\Upsilon_\beta)\begin{bmatrix} 0 \\ s \\ 0 \end{bmatrix} = \mathbf{R}_x(\Upsilon)\mathbf{R}_z(\Lambda)\begin{bmatrix} 0 \\ s \\ 0 \end{bmatrix}, \tag{A1}$$

where $\mathbf{R}_y(90° - \beta)$ pitches the stroke plane away from vertical to instead be along the stroke angle β and $\mathbf{R}_x(\Upsilon_\beta)$ adds the component of the dihedral Υ_β within the inclined stroke plane, rather than Υ in the yz plane. By matching matrix terms we obtain

$$\Lambda = -\arctan(\cot \beta \sin \Upsilon), \tag{A2}$$

$$\Upsilon_\beta = \arcsin \frac{-\sin \Lambda}{\cos \beta}. \tag{A3}$$

APPENDIX B: FLOW ANGLE DETERMINATION

The position $\mathbf{r}_g(s,t)$ of the quarter-chord axis in the global frame is

$$\mathbf{r}^g(s,t) = \begin{bmatrix} -Ut \\ 0 \\ 0 \end{bmatrix} + \mathbf{R}_b^g(\Lambda,\Upsilon,\theta)\begin{bmatrix} c/4 \\ s \\ 0 \end{bmatrix}. \tag{B1}$$

Next we can determine the flow angle, defined as the direction of oncoming flow if the entire wing has zero pitch rotation $\theta(s,t) = 0$. The flow angle is derived from the global frame motion $\dot{\mathbf{r}}^g$ projected onto the x and z body frame axes

$$\theta_{\text{flow}}(s,t) = \arctan \frac{\dot{\mathbf{r}}^g \cdot \mathbf{R}_b^g(\Lambda,\Upsilon,0)\,\hat{\mathbf{z}}^b}{-\dot{\mathbf{r}}^g \cdot \mathbf{R}_b^g(\Lambda,\Upsilon,0)\,\hat{\mathbf{x}}^b}, \tag{B2}$$

where $\hat{\mathbf{x}}^b = [1\,0\,0]^T$ and $\hat{\mathbf{z}}^b = [0\,0\,1]^T$ are the body frame axes. Given the lack of pitch rotation for this quantity, the offset $c/4$ can also be safely ignored when determining the flow angle at the wing tip since $R \gg c/4$. The angle of attack α at quarter chord is now simply the difference between the pitch θ and flow angle θ_{flow}:

$$\alpha(s,t) = \theta(s,t) - \theta_{\text{flow}}(s,t). \tag{B3}$$

Finally, when computing the lift from this angle of attack, the flow velocity along the span is ignored in order to account for wing sweep [43]. The effective flow speed V perpendicular to the span is therefore

$$V(s,t) = \sqrt{\left[\dot{\mathbf{r}}^g \cdot \mathbf{R}_b^g(\Lambda,\Upsilon,0)\hat{\mathbf{z}}^b\right]^2 + \left[-\dot{\mathbf{r}}^g \cdot \mathbf{R}_b^g(\Lambda,\Upsilon,0)\hat{\mathbf{x}}^b\right]^2}, \tag{B4}$$

where once again we project the total motion total motion $\dot{\mathbf{r}}^g$ onto the x and z body frame axes.

APPENDIX C: CRANKSHAFT EQUATIONS

The crankshaft rotates at constant angular rate ω, as is standard in ornithopter design (easing future integration of our experiment into a robotic solution), forcing the wing dihedral angle $\Upsilon(t) = 45° \cos[\phi(t)]$ to oscillate. However, given the crankshaft mechanism equations, the dihedral motion is not a pure sinusoid, as $\phi(t) \neq \omega t$. The deviation from a pure sinusoid is small, and as illustrated in the main text, feedback optimization effectively removes imperfections in the force

response. Additionally, the use of a crankshaft, possibly the most common method for efficiently generating oscillatory motion, illustrates the robustness of the phenomena involved to correct motion perturbations.

The exact expression for the dihedral phase $\phi(t)$ was used throughout the motion planning, data processing, and modeling and is derived as follows. Given a crank of radius r_{crank} offset from the dihedral axis x by z_{crank} and y_{crank}, the motion of the wing dihedral $\Upsilon(t)$ is

$$\Upsilon(t) = \arctan\left[\frac{z_{\text{crank}} - r_{\text{crank}}\sin(\omega t)}{y_{\text{crank}} - r_{\text{crank}}\cos(\omega t)}\right] + \arccos\left[\frac{l_{\text{linkage}}^2 - h(t)^2 - l_{\text{lever}}^2}{2l_{\text{lever}}h(t)}\right], \quad (C1)$$

where $l_{\text{linkage}} = 7.7$ cm is the linkage length, $l_{\text{lever}} = 6.5$ cm is the lever length, $r_{\text{crank}} = 4.4$ cm, $y_{\text{crank}} = 8.5$ cm, $z_{\text{crank}} = 2.3$ cm, and $h(t)$ is the distance from the crank tip to the dihedral axis

$$h(t) = \sqrt{[z_{\text{crank}} - r_{\text{crank}}\sin(\omega t)]^2 + [y_{\text{crank}} - r_{\text{crank}}\cos(\omega t)]^2}. \quad (C2)$$

Finally, we can define the dihedral phase ϕ as the true phase of the flapping

$$\phi(t) = \arccos\frac{\Upsilon(t)}{\max[\Upsilon(t)]}. \quad (C3)$$

[1] J. M. Anderson, K. Streitlien, D. S. Barrett, and M. S. Triantafyllou, Oscillating foils of high propulsive efficiency, J. Fluid Mech. **360**, 41 (1998).

[2] D. A. Read, F. S. Hover, and M. S. Triantafyllou, Forces on oscillating foils for propulsion and maneuvering, J Fluid. Struct. **17**, 163 (2003).

[3] M. W. Rosen, *Experiments with Swimming Fish and Dolphins* (American Society of Mechanical Engineers, New York, 1961).

[4] G. K. Taylor, R. L. Nudds, and A. L. R. Thomas, Flying and swimming animals cruise at a Strouhal number tuned for high power efficiency, Nature (London) **425**, 707 (2003).

[5] M. Gazzola, M. Argentina, and L. Mahadevan, Scaling macroscopic aquatic locomotion, Nat. Phys. **10**, 758 (2014).

[6] M. M. Koochesfahani, Vortical patterns in the wake of an oscillating airfoil, AIAA J. **27**, 1200 (1989).

[7] M. J. Wolfgang, J. M. Anderson, M. A. Grosenbaugh, D. K. Yue, and M. S. Triantafyllou, Near-body flow dynamics in swimming fish, J. Exp. Biol. **202**, 2303 (1999).

[8] S. Heathcote, Z. Wang, and I. Gursul, Effect of spanwise flexibility on flapping wing propulsion, J Fluid. Struct. **24**, 183 (2008).

[9] A. H. Techet, Propulsive performance of biologically inspired flapping foils at high Reynolds numbers, J. Exp. Biol. **211**, 274 (2008).

[10] F. S. Hover, Ø. Haugsdal, and M. S. Triantafyllou, Effect of angle of attack profiles in flapping foil propulsion, J Fluid. Struct. **19**, 37 (2004).

[11] M. S. Triantafyllou, A. H. Techet, and F. S. Hover, Review of experimental work in biomimetic foils, IEEE J. Ocean. Eng. **29**, 585 (2004).

[12] S. C. Licht, M. S. Wibawa, F. S. Hover, and M. S. Triantafyllou, In-line motion causes high thrust and efficiency in flapping foils that use power downstroke, J. Exp. Biol. **213**, 63 (2010).

[13] B. Tobalske and K. Dial, Flight kinematics of black-billed magpies and pigeons over a wide range of speeds, J. Exp. Biol. **199**, 263 (1996).

[14] U. M. L. Norberg and Y. Winter, Wing beat kinematics of a nectar-feeding bat, *Glossophaga soricina*, flying at different flight speeds and strouhal numbers, J. Exp. Biol. **209**, 3887 (2006).

[15] J. M. Wakeling and C. P. Ellington, Dragonfly flight. II. Velocities, accelerations and kinematics of flapping flight, J. Exp. Biol. **200**, 557 (1997).

[16] J. Davenport, S. A. Munks, and P. J. Oxford, A comparison of the swimming of marine and freshwater turtles, Proc. R. Soc. London Ser. B **220**, 447 (1984).

[17] B. G. Szymik and R. A. Satterlie, Changes in wingstroke kinematics associated with a change in swimming speed in a pteropod mollusk, Clione limacina, J. Exp. Biol. **214**, 3935 (2011).

[18] J. S. Izraelevitz and M. S. Triantafyllou, Adding in-line motion and model-based optimization offers exceptional force control authority in flapping foils, J. Fluid Mech. **742**, 5 (2014).

[19] J. S. Izraelevitz and M. S. Triantafyllou, *Proceedings of the 2015 IEEE International Conference on Robotics and Automation (ICRA)* (IEEE, Piscataway, 2015), p. 5830.

[20] K. H. Elliott, R. E. Ricklefs, A. J. Gaston, S. A. Hatch, J. R. Speakman, and G. K. Davoren, High flight costs, but low dive costs, in auks support the biomechanical hypothesis for flightlessness in penguins, Proc. Natl. Acad. Sci. USA **110**, 9380 (2013).

[21] C. J. Pennycuick, Flight of auks (Alcidae) and other northern seabirds compared with southern Procellariiformes: Ornithodolite observations, J. Exp. Biol. **128**, 335 (1987).

[22] J. Arfaoui, Flying herring gull, 2009 (accessed online 25 April 2017; Creative Commons Attribution-Share Alike 3.0 Unported).

[23] funtopia.tv, horned puffin, 2012 (accessed online from Flickr 19 April 2017; Creative Commons Attribution-NonCommercial-NoDerivs 2.0 Generic 2.0 Generic).

[24] J. More, Puffin 17, 2016 (accessed online from Flickr 19 April 2017; Creative Commons Attribution-NonCommercial-NoDerivs 2.0 Generic 2.0 Generic).

[25] E. Kim, Little blue penguins at NEAQ, Boston, 2013 (accessed online from Flickr 19 April 2017; Creative Commons Attribution 2.0 Generic).

[26] M. P. Harris and S. Wanless, *The Puffin* (Bloomsbury, London, 2011), p. 110.

[27] L. C. Johansson and B. S. W. Aldrin, Kinematics of diving atlantic puffins (*Fratercula arctica* L.): Evidence for an active upstroke, J. Exp. Biol. **205**, 371 (2002).

[28] P. R. Stettenheim, Adaptations for underwater swimming in the common murre (Uria aalge), Ph.D. thesis, University of Michigan, 1974.

[29] Available at https://openclipart.org.

[30] B. W. Tobalske, D. R. Warrick, C. J. Clark, D. R. Powers, T. L. Hedrick, G. A. Hyder, and A. A. Biewener, Three-dimensional kinematics of hummingbird flight, J. Exp. Biol. **210**, 2368 (2007).

[31] Y. Watanuki, S. Wanless, M. Harris, J. R. Lovvorn, M. Miyazaki, H. Tanaka, and K. Sato, Swim speeds and stroke patterns in wing-propelled divers: A comparison among alcids and a penguin, J. Exp. Biol. **209**, 1217 (2006).

[32] J. M. Rayner, *Symposia of the Society for Experimental Biology* (Company of Biologists, Cambridge, 1995), Vol. 49, pp. 131–155.

[33] J. R. Lovvorn, Y. Watanuki, A. Kato, Y. Naito, and G. A. Liggins, Stroke patterns and regulation of swim speed and energy cost in free-ranging Brünnich's guillemots, J. Exp. Biol. **207**, 4679 (2004).

[34] J. R. Lovvorn and D. R. Jones, Biomechanical conflicts between adaptations for diving and aerial flight in estuarine birds, Estuaries Coasts **17**, 62 (1994).

[35] S. F. Hoerner, *Fluid-Dynamic Drag: Practical Information on Aerodynamic Drag and Hydrodynamic Resistance* (Hoerner Fluid Dynamics, Midland Park, 1965).

[36] S. Vogel, *Life in Moving Fluids: The Physical Biology of Flow* (Princeton University Press, Princeton, 1994).

[37] D. M. Kikuchi, Y. Watanuki, N. Sato, K. Hoshina, A. Takahashi, and Y. Y. Watanabe, Strouhal number for flying and swimming in rhinoceros auklets *Cerorhinca monocerata*, J. Avian Biol. **46**, 406 (2015).

[38] J. Bédard, Adaptive radiation in alcidae, Ibis **111**, 189 (1969).

[39] R. J. Lock, R. Vaidyanathan, and S. C. Burgess, Impact of marine locomotion constraints on a bio-inspired aerial-aquatic wing: Experimental performance verification, J. Mech. Robot. **6**, 1 (2014).

[40] C. J. Pennycuick, *Modelling the Flying Bird*, Theoretical Ecology Series Vol. 5 (Academic, New York, 2008), pp. 105–128.

[41] J. Izraelevitz and M. Triantafyllou, Adjustable linkage mechanism for varying stroke angle in flapping aerial/aquatic vehicle, U.S. Provisional Patent Application No. 62/069467 (pending).

[42] A. Slaouti and J. H. Gerrard, An experimental investigation of the end effects on the wake of a circular cylinder towed through water at low Reynolds numbers, J. Fluid Mech. **112**, 297 (1981).

[43] S. F. Hoerner and H. V. Borst, *Fluid-Dynamic Lift: Practical Information on Aerodynamic and Hydrodynamic Lift* (Hoerner Fluid Dynamics, Brick Town, 1985).

[44] R. Featherstone, *Rigid Body Dynamics Algorithms* (Springer, New York, 2008), Vol. 49.

[45] T. Theodorsen, General theory of aerodynamic instability and the mechanism of flutter, Langley Aeronautical Laboratory Technical Report No. NACA-TR-496, 1949.

[46] J. S. Izraelevitz, Q. Zhu, and M. S. Triantafyllou, State-space adaptation of unsteady lifting line theory: Twisting/flapping wings of finite span, AIAA J. **55**, 1279 (2017).

[47] J. O. Scherer, Experimental and theoretical investigation of large amplitude oscillation foil propulsion systems, Defense Technical Information Center Technical Report No. TR-662-1-F, 1968.

[48] H. Wagner, Über die entstehung des dynamischen auftriebes von tragflügeln, ZAMM-Z. Angew. Math. Mech. **5**, 17 (1925).

[49] J. M. V. Rayner, A vortex theory of animal flight. Part 2. The forward flight of birds, J. Fluid Mech. **91**, 731 (1979).